nature communications

Article

https://doi.org/10.1038/s41467-024-51472-w

Effects of surface hydrophobization on the phase evolution behavior of iron-based catalyst during Fischer–Tropsch synthesis

Received: 14 March 2024

Accepted: 8 August 2024

Yanfei Xu[1,2], Zhenxuan Zhang[1], Ke Wu[1], Jungang Wang[3], Bo Hou[3], Ruoting Shan[1], Ling Li[1] & Mingyue Ding[1,4]

Iron-based Fischer–Tropsch synthesis (FTS) catalyst is widely used for syngas conversion, but its iron carbide active phase is easily oxidized into Fe_3O_4 by the water produced during reaction, leading to the deterioration of catalytic performance. Here, we show an efficient strategy for protecting the iron carbide active phase of FTS catalyst by surface hydrophobization. The hydrophobic surface can reduce the water concentration in the core vicinity of catalyst during syngas conversion, and thus inhibit the oxidation of iron species by water, which enhances the C − C coupling ability of catalyst and promotes the formation of long-chain olefins. More significantly, it is unraveled that appropriate shell thickness plays a crucial role in stabilizing the iron carbide active phase without Fe_3O_4 formation and achieving good catalytic performance.

Converting syngas ($CO + H_2$) into chemicals and liquid fuels via the Fischer–Tropsch synthesis (FTS) reaction serves as a competitive alternative to the traditional petroleum route, since syngas can be directly derived from renewable biomass, plentiful coal and natural gas. Developing efficient FTS catalyst has received much-renewed interests in recent years[1–7]. Compared with cobalt and ruthenium, the iron-based catalyst has great advantages in the industrial FTS process, on account of its flexible product distribution, wide reaction conditions, and low price. During reaction, the carbon atom in CO is hydrogenated to form hydrocarbons, and the oxygen atom is released as H_2O[8,9]. Since the iron species are easily carbonized by CO and oxidized by H_2O at the FTS reaction conditions, the iron-based catalyst generally evolves into a mixture of iron carbide and Fe_3O_4 phases during syngas conversion[10–12]. Iron carbide phase is responsible for the CO activation and C − C coupling processes for producing multi-carbon hydrocarbons, while Fe_3O_4 phase is very active for the side reaction related to CO_2 formation[13,14]. Therefore, protecting iron carbide from oxidation during syngas conversion is highly desirable.

Zhao et al. [15] successfully synthesized a range of FTS catalysts with pure-phase Fe, Fe_5C_2, Fe_7C_3, and Fe_2C, respectively. Whereas, these iron species were gradually oxidized into Fe_3O_4 phase during reaction, resulting in the deterioration of catalytic performance with time on stream. Cheng et al. [16] effectively suppressed Fe_3O_4 formation via enhancing the carburization process of iron-based catalyst by the dual decoration of Mg and K, but excessive promoter led to the coverage of active sites and activity drop. Gong et al. [17] reported that Sn could reduce the adsorption energy of chemisorbed oxygen and thus avoid the oxidation of iron carbide structure, however the easy migration of Sn to catalyst surface blocked the active sites excessively. Emiel J. M. Hensen et al. [18] synthesized pure-phase Fe_2C via a precisely controlled carburization process, and this iron carbide phase was durable at 235 °C and CO conversion of 15%. Stabilizing iron carbide at relatively high reaction temperature and CO conversion level during syngas conversion is still very challenging.

Considering the formation of Fe_3O_4 is attributed to the oxidation of iron species by H_2O, inhibiting the adsorption of H_2O on catalyst is a promising method to protect iron carbide during reaction. In our previous work[19], we proposed a strategy to hinder the adsorption of H_2O and restrain the side reactions related to H_2O by making the catalyst surface hydrophobic, which has been applied successfully to the reactions of syngas conversion to light olefins[20,21], dimethyl ether[22], higher alcohol[23], and high-quality gasoline[24]. Zhang et al. [25] reported that the Fe_5C_2/Fe_3O_4 ratio in catalyst during reaction could be adjusted by altering the hydrophobic degree of catalyst surface. Liu et al. [26] found

---

[1] School of Power and Mechanical Engineering, Wuhan University, Wuhan 430072, China. [2] Suzhou Institute of Wuhan University, Suzhou 215125, China. [3] State Key Laboratory of Coal Conversion, Institute of Coal Chemistry, Chinese Academy of Sciences, Taiyuan 030001, China. [4] Academy of Advanced Interdisciplinary Studies, Wuhan University, Wuhan 430072, China. e-mail: yanfei_xu@whu.edu.cn; dingmy@whu.edu.cn

that the hydrophobic surface could inhibit Fe_3O_4 formation and stabilize iron carbide, especially the Fe_7C_3 phase, while Yu et al.[27] reported that the hydrophobic catalyst was mainly consisted of Fe_3O_4 phase after syngas conversion. The phase transformation of iron species during reaction is complex, and the effects of surface hydrophobization on the phase evolution behavior of iron-based catalyst are still elusive.

Herein, we investigated the role of hydrophobic surface on tuning the phase composition and catalytic performance of iron-based FTS catalyst in detail. It was discovered that the hydrophobic shell could reduce the water concentration in the core vicinity of catalyst during syngas conversion, thereby inhibiting the oxidation of iron species by water and enhancing the conversion of syngas to long-chain olefins. In addition, appropriate thickness of hydrophobic shell was crucial to stabilize the iron carbide active phase without the formation of Fe_3O_4 phase.

Results

Structural characterization and catalytic performance

The synthesis steps of hydrophilic and hydrophobic catalysts were shown in Supplementary Fig. 1. Fe_2O_3 nanoparticle was synthesized by a hydrothermal method, and Mn promoter was deposited on Fe_2O_3 surface via deposition-precipitation. The hydrophilic SiO_2-coated catalyst (Fe@Mn@*x*Si) was obtained by the controllable hydrolysis of *x* mL of tetraethyl orthosilicate (TEOS) on Fe@Mn. Transmission electron microscope (TEM) images and corresponding energy dispersive X-ray spectroscopy (EDS) elemental mapping confirmed that Fe@Mn nanoparticle was coated homogeneously by amorphous SiO_2 (Supplementary Fig. 2). Besides, the content and thickness of SiO_2 shell were effectively adjusted by altering the dosage of TEOS (Supplementary Table 1). The hydrophobic SiO_2-coated catalyst (Fe@Mn@*x*Si-c) was further prepared via the surface silanization treatment (Supplementary Figs. 3–6).

After the FTS reaction, the FeMn species were still well encapsulated by the SiO_2 shell (Fig. 1a–f). Notably, the core of the Fe@Mn@0.2Si-c catalyst shrank obviously compared with the Fe@Mn@0.2Si catalyst. Considering the spatial dimensions of different iron phases vary greatly (Supplementary Fig. 7 and Supplementary Table 2), the change in core size of catalyst reflected the phase evolution of iron species during reaction. The detailed phase composition of catalyst was further characterized by X-ray diffraction (XRD) and Mössbauer spectrum (Supplementary Figs. 8,9 and Supplementary Table 3). During reaction, the Fe_2O_3 phase in the hydrophilic Fe@Mn@0.2Si catalyst was transformed into a mixture of 59.7% χ-Fe_5C_2, 34.3% Fe_3O_4 and 6.0% Fe^{3+}(spm), while that in the hydrophobic

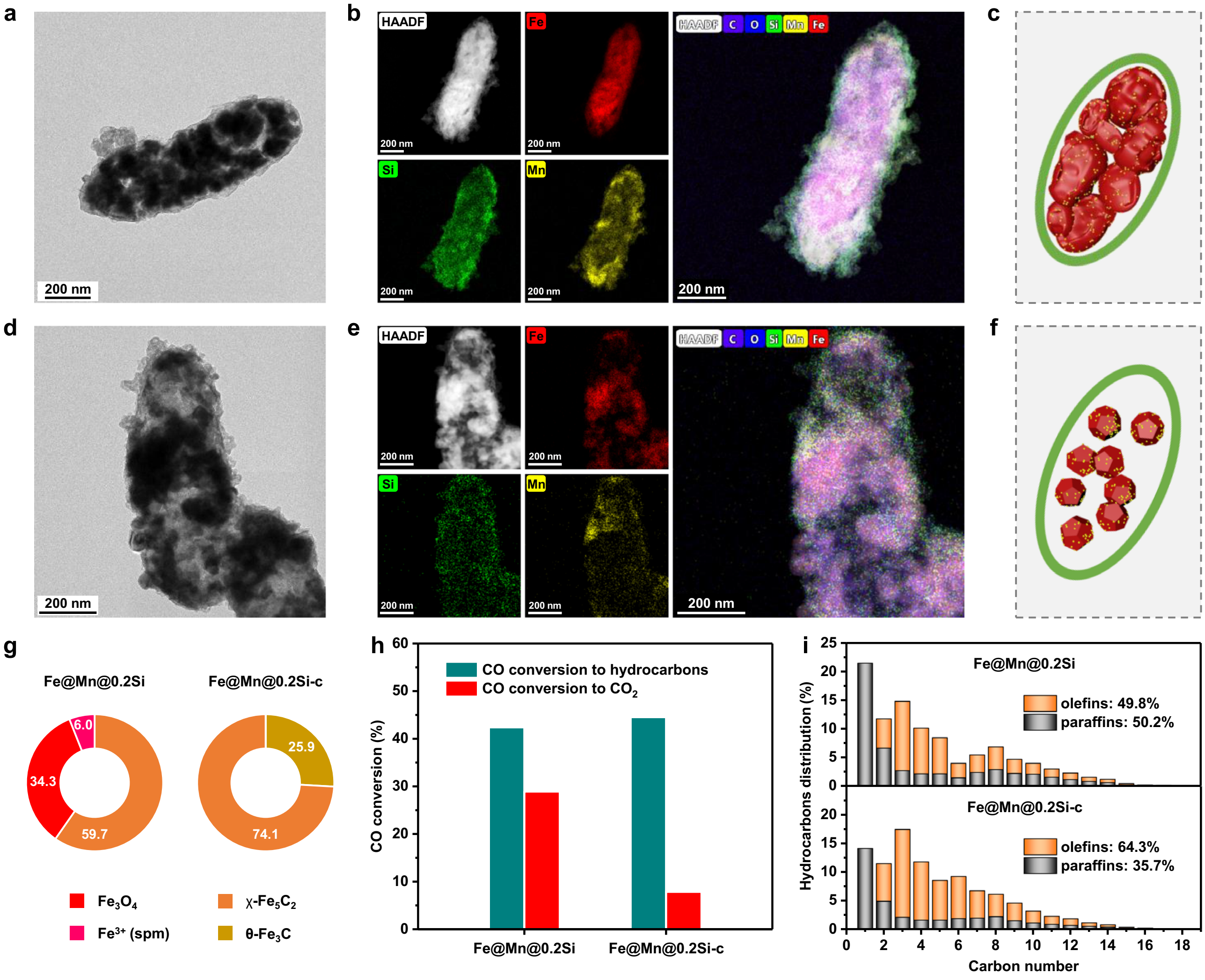

Fig. 1 | Structural characterization and catalytic performance. a–**c** TEM image (**a**), EDS elemental mapping (**b**), and structural model (**c**) of the spent Fe@Mn@0.2Si catalyst. **d**–**f** TEM image (**d**), EDS elemental mapping (**e**), and structural model (**f**) of the spent Fe@Mn@0.2Si-c catalyst. **g** Phase composition of the spent catalysts determined by Mössbauer spectroscopy. **h**, **i** CO conversion (**h**) and hydrocarbons distribution (**i**) of the Fe@Mn@0.2Si and Fe@Mn@0.2Si-c catalysts.

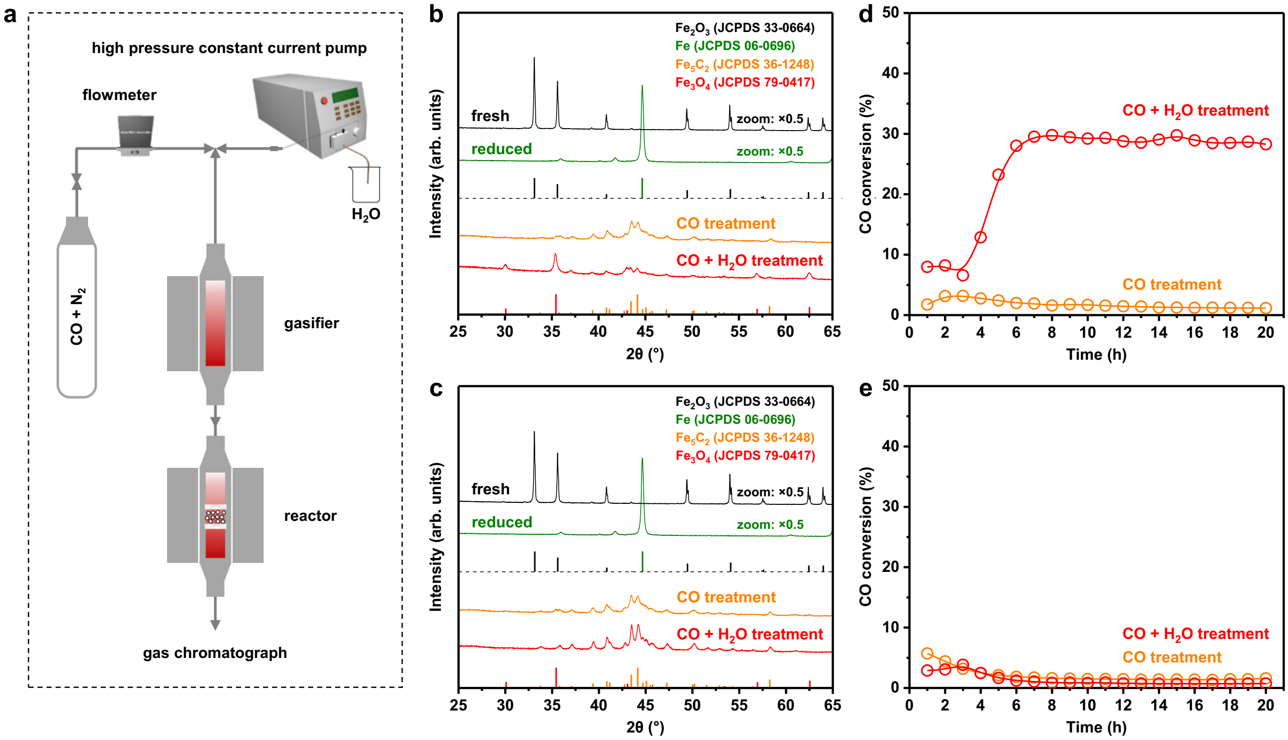

Fig. 2 | Phase evolution behaviors of the hydrophilic and hydrophobic catalysts. a The schematic diagram of the CO + H_2O model experiment. Firstly, the catalyst was reduced in pure H_2 at 350 °C, 0.1 MPa for 20 h. Subsequently, the catalyst was exposed to the CO or CO + H_2O atmosphere at 320 °C, 2.0 MPa for 20 h. **b**, **c** XRD patterns of the Fe@Mn@0.2Si (**b**) and Fe@Mn@0.2Si-c (**c**) catalysts at different stages. **d**, **e** CO conversion of the Fe@Mn@0.2Si (**d**) and Fe@Mn@0.2Si-c (**e**) catalysts during the model experiment.

Fe@Mn@0.2Si-c catalyst was converted into 74.1% χ-Fe_5C_2 and 25.9% θ-Fe_3C (Fig. 1g). These results suggested that the surface hydrophobization had obvious effects on the phase evolution behavior of iron-based FTS catalyst during syngas conversion.

Since hydrocarbon products are produced on iron carbide (Fe_xC) rather than Fe_3O_4[18,19], the phase composition of catalyst obviously influenced the catalytic performances (Fig. 1h, i). The selectivity of CH_4 in hydrocarbons decreased from 21.5% on the Fe@Mn@0.2Si catalyst to 14.1% on the Fe@Mn@0.2Si-c catalyst, accompanied with the increase of olefins selectivity from 49.8% to 64.3%, implying the enhancement of C − C coupling ability and inhibition of olefins hydrogenation activity during syngas conversion. In addition, the CO conversion to CO_2 on the Fe@Mn@0.2Si catalyst was 28.9%, while that on the Fe@Mn@0.2Si-c catalyst was only 7.9%, which was attributed to that the hydrophobic shell inhibited water adsorption and hindered the water-gas shift (WGS) side reaction related to CO_2 formation[19,24]. Moreover, the Fe@Mn@0.2Si-c catalyst presented a good catalytic stability during 110 hours of continuous reaction (Supplementary Fig. 10). The above results displayed the importance of surface hydrophobization in stabilizing the Fe_xC active phase for enhancing olefins production.

Insights into the phase evolution behavior of catalyst

To illustrate the regulation effect of hydrophobic surface on the phase composition of catalyst, we investigated the phase evolution behaviors of the hydrophilic Fe@Mn@0.2Si and hydrophobic Fe@Mn@0.2Si-c catalysts in the CO + H_2O model experiment under the reaction temperature and pressure of syngas conversion (Fig. 2a). The Fe_2O_3 phase in the two catalysts was reduced into metallic iron (Fe^0) phase by reducing in pure H_2 (Fig. 2b, c). After switching to the CO atmosphere, a low CO conversion of about 5% was observed, which decreased continuously with time on stream (Fig. 2d, e). Moreover, only Fe_5C_2 phase was detected in the two catalysts after the CO treatment, suggesting that CO molecules could diffuse through the hydrophilic and hydrophobic SiO_2 shell and thus carbonize the internal Fe^0 phase.

When co-feeding CO and H_2O in the reactor, the CO conversion of the Fe@Mn@0.2Si catalyst reached about 30% (Fig. 2d) and a mixture of Fe_3O_4 and Fe_5C_2 phases was detected (Fig. 2b), implying that H_2O molecules could easily diffuse through the hydrophilic SiO_2 shell and thus oxidize internal iron species. By contrast, the stable CO conversion of the Fe@Mn@0.2Si-c catalyst was less than 2% (Fig. 2e) and no Fe_3O_4 phase was detected after the CO + H_2O treatment (Fig. 2c). As illustrated in our previous work[24], the diffusion of water molecules through hydrophilic SiO_2 is bidirectional, while the diffusion through hydrophobic SiO_2 is unidirectional. Thus, the H_2O molecules outside catalyst ($H_2O_{outside}$) could hardly diffuse in and influence the phase composition of the hydrophobic Fe@Mn@0.2Si-c catalyst. During syngas conversion, even though H_2O molecules were produced on the internal Fe_xC active sites, the hydrophobic surface hindered the entry of $H_2O_{outside}$, which reduced the water concentration in the core vicinity of catalyst. Thus, surface hydrophobization of catalyst could inhibit the oxidation of iron species and stabilize the Fe_xC active phase during reaction.

To further illustrate the protective effect of hydrophobic surface on iron carbide, in situ XRD characterizations on the Fe@Mn@0.2Si and Fe@Mn@0.2Si-c catalysts in the CO + H_2O atmosphere were conducted. Before test, the iron species in the two catalysts were transformed into iron carbide by the H_2 reduction and CO carbonization procedures in Fig. 2. Then, the two catalysts were exposed to the CO + H_2O atmosphere at 320 °C to observe the influence of H_2O on the iron carbide in the two catalysts. As shown in Fig. 3a, the iron carbide in the hydrophilic Fe@Mn@0.2Si catalyst gradually evolved once introducing H_2O into the reactor chamber. With time on stream, the intensity of diffraction peaks related to iron carbide decreased, while new diffraction peaks at 35.4°, 57.0°, and 62.5° attributed to Fe_3O_4 phase appeared (Fig. 3b). In addition, the phase evolution proceeded

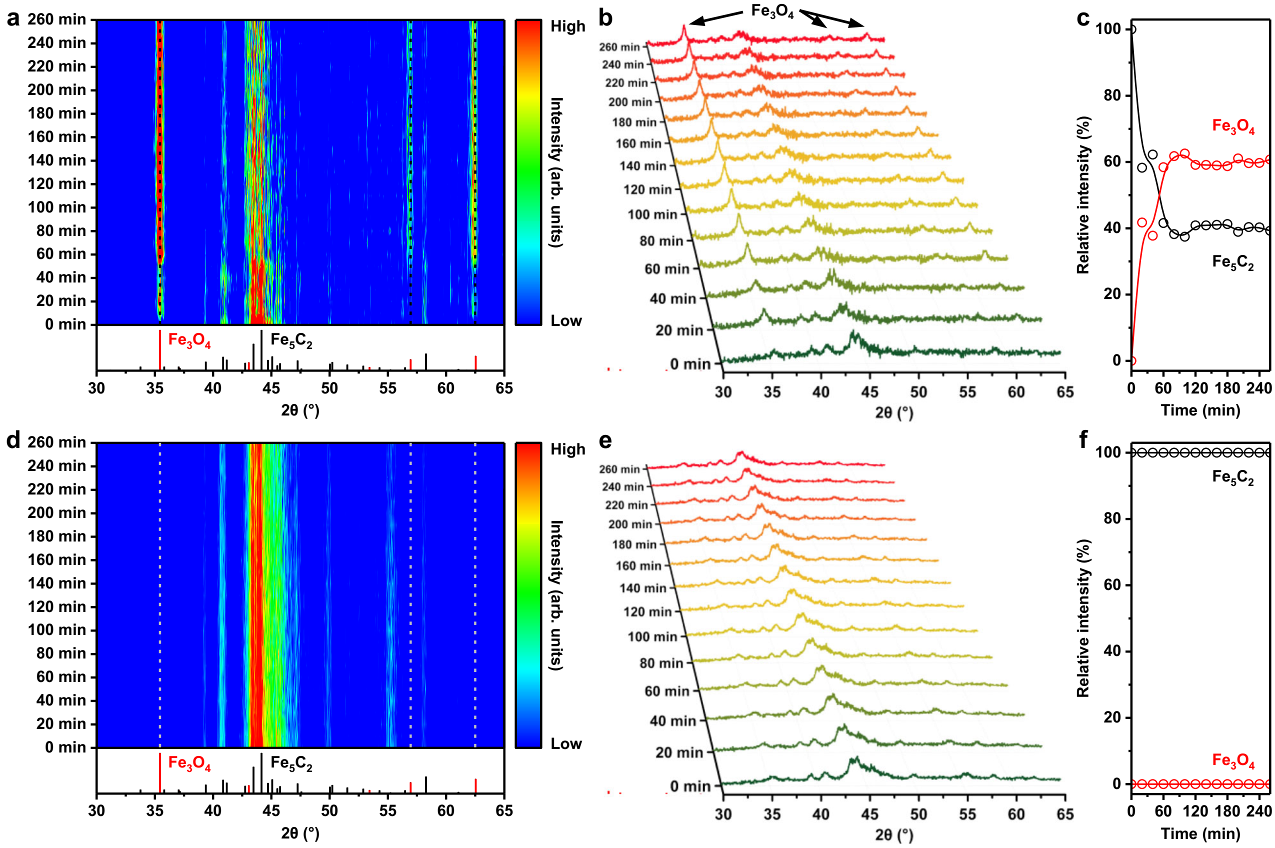

Fig. 3 | Inhibiting the oxidation of iron carbide by water via surface hydrophobization. **a**–**c** Heatmap (**a**), in situ XRD patterns (**b**), and the relative intensity between the diffraction peak of Fe_5C_2 at 44.2° and the diffraction peak of Fe_3O_4 at 35.4° (**c**) of the Fe@Mn@0.2Si catalyst when exposing to the CO + H_2O atmosphere at 320 °C. **d**–**f** Heatmap (**d**), in situ XRD patterns (**e**), and the relative intensity between the diffraction peak of Fe_5C_2 at 44.2° and the diffraction peak of Fe_3O_4 at 35.4° (**f**) of the Fe@Mn@0.2Si-c catalyst when exposing to the CO + H_2O atmosphere at 320 °C.

rapidly and reached an equilibrium state within one hour (Fig. 3c). These results suggested that H_2O molecules adsorbed easily on the hydrophilic Fe@Mn@0.2Si catalyst and thereby oxidized the internal iron carbide into Fe_3O_4 phase. As for the hydrophobic Fe@Mn@0.2Si-c catalyst, this phase evolution process was not observed (Fig. 3d). With time on stream, the intensity of diffraction peaks related to iron carbide in this hydrophobic catalyst remained stable and no diffraction peak related to Fe_3O_4 phase was detected (Fig. 3e, f). The above results of in situ XRD characterization clearly demonstrated the different phase evolution process of iron carbide in the hydrophilic Fe@Mn@0.2Si and hydrophobic Fe@Mn@0.2Si-c catalysts when exposing to the CO + H_2O atmosphere, confirming that the oxidation of iron carbide by H_2O molecules could be effectively inhibited via surface hydrophobization.

Effects of shell thickness on the phase structure and catalytic performance

The effects of the thickness of SiO_2 shell on the reduction-carburization behaviors of internal iron species in catalyst were characterized by carbon monoxide temperature-programmed reduction (CO-TPR). As the increase of TEOS dosage, the reduction peaks shifted towards higher temperature and the peaks area gradually decreased (Supplementary Fig. 11), suggesting that the increase of shell thickness inhibited the accessibility and carburization of internal iron species by CO molecules. Therefore, after the FTS reaction, the content of Fe_xC phase in catalyst reduced while that of Fe_3O_4 phase obviously increased with the thickening of SiO_2 shell (Supplementary Fig. 12). As Fe_xC phase was the active site for FTS reaction, the CO conversion to hydrocarbons decreased obviously from 53.8% of Fe@Mn@0.05Si to 24.3% of Fe@Mn@2.8Si (Fig. 4a). The increase of shell thickness did not inhibit the accessibility of internal iron species by H_2 due to the much smaller size of hydrogen molecule (Supplementary Fig. 13), which would lead to a higher H_2/CO ratio in the core locality of catalyst and enhance the hydrogenation reaction. As a result, the hydrocarbons distribution shifted towards lower carbon number and the olefins selectivity in hydrocarbons decreased from 66.8% of Fe@Mn@0.05Si to 27.1% of Fe@Mn@2.8Si (Fig. 4c and Supplementary Fig. 14). All the hydrophilic Fe@Mn@xSi catalysts exhibited high CO_2 selectivity of about 40%, suggesting that H_2O produced by the FTS reaction participated easily in the WGS side reaction (Supplementary Fig. 15).

As discussed above, although H_2O was produced on internal Fe_xC during syngas conversion, the hydrophobic surface could restrict the entry of $H_2O_{outside}$, thereby reducing the water concentration in the core vicinity of catalyst (Figs. 2, 3). Therefore, the WGS side reaction was hindered and the oxidation of iron species by H_2O was inhibited (Supplementary Fig. 16 and Fig. 1). The increase of SiO_2 shell thickness inhibited the accessibility and carburization process of internal iron species by CO molecules, leading to the slight oxidation of iron species before $H_2O_{intside}$ diffused outside the Fe@Mn@0.5Si-c and Fe@Mn@1.0Si-c catalysts (Supplementary Fig. 17). With the gradually thickening of SiO_2 shell, the catalytic activity and hydrocarbons distribution of the hydrophobic catalysts presented similar trend with that of the hydrophilic catalysts (Fig. 4b, d and Supplementary Fig. 18). Exceptionally, the Fe@Mn@0.05Si-c catalyst coated with the thinnest SiO_2 shell exhibited low CO conversion of < 2% (Fig. 4b), and only Fe_3O_4 phase was detected in the spent Fe@Mn@0.05Si-c catalyst (Fig. 4e and Supplementary Fig. 19), suggesting that there was other factor that could inhibit the carbonization of iron species.

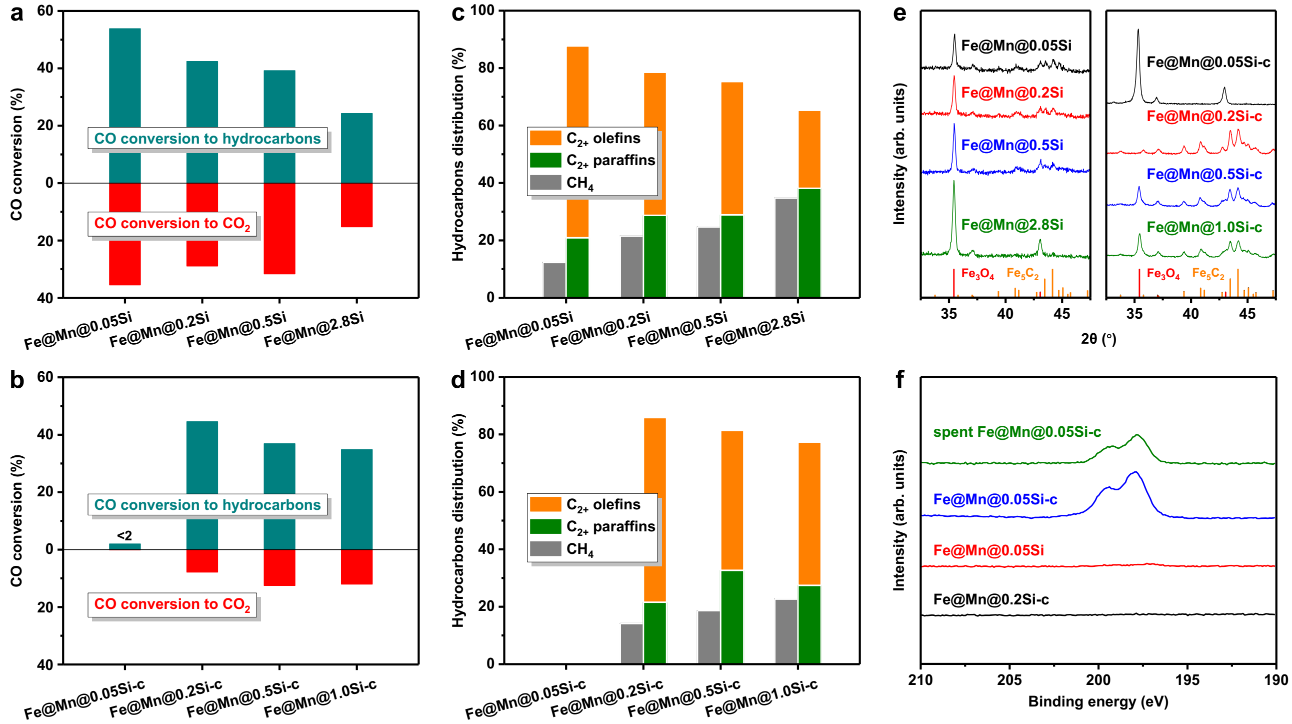

Fig. 4 | Effects of shell thickness on the phase structure and catalytic performance. **a**, **b** CO conversion of the Fe@Mn@*x*Si (**a**) and Fe@Mn@*x*Si-c (**b**) catalysts. **c**, **d** Hydrocarbons distribution of the Fe@Mn@*x*Si (**c**) and Fe@Mn@*x*Si-c (**d**) catalysts. **e** XRD patterns of the spent catalysts. **f** XPS spectra of Cl 2*p* on catalysts.

Poisoning effect of chlorine on the phase evolution

We noticed that chlorine element existed on the Fe@Mn@0.05Si-c catalyst, which was attributed to hydrogen chloride produced during the hydrophobic modification process using chlorotrimethylsilane (Supplementary Fig. 3). Chlorine could not be removed by the washing and vacuum drying procedures of catalyst synthesis and even the reaction at high temperature (Fig. 4f), due to its strong adsorption on the catalyst surface[28–30]. The existence of chlorine on catalyst surface reduced obviously the CO conversion (Supplementary Figs. 20, 21). Sulfur, ammonia and halogen compounds can behave as catalyst poisons and lead to the deactivation of FTS catalyst[31–33]. However, the mechanism of chlorine poisoning of the iron-based catalyst is still unclear. In industry, syngas derived from coal, especially biomass, generally contains chlorine impurity, which presents in the form of hydrogen chloride[33–35]. Thus, the form of chlorine studied in this work is similar to those in real process, and understanding the poisoning mechanism of chlorine on catalyst is also important for the industrial application.

To understand the influence of chlorine on the formation of Fe_xC active phase, in situ XRD characterizations on the Fe@Mn@0.05Si and Fe@Mn@0.05Si-c catalysts in the 10%CO/90%N_2 atmosphere were conducted. With the increase of temperature, the phase composition of the Fe@Mn@0.05Si catalyst gradually evolved (Fig. 5b). The Fe_2O_3 phase was converted into Fe_3O_4 phase at 350 °C, which was transformed rapidly into FeO phase at 400 °C. Subsequently, Fe_5C_2 phase appeared at 500 °C. These results revealed the carbonization path of $Fe_2O_3 \rightarrow Fe_3O_4 \rightarrow FeO \rightarrow Fe_5C_2$ of iron species, and this phase evolution process proceeded easily in the Fe@Mn@0.05Si catalyst with an initial transformation temperature of 350 °C. However, as for the Fe@Mn@0.05Si-c catalyst, the Fe_2O_3 phase was only converted slightly into Fe_3O_4 phase without the formation of Fe_xC phase even at high temperature of 500 °C (Fig. 5c). The above results suggested that CO could hardly influence the phase composition of the Fe@Mn@0.05Si-c catalyst, thus no Fe_xC active phase was formed during syngas conversion and the CO conversion was less than 2% (Fig. 5a).

To shed light on the reason of different phase evolution processes between the Fe@Mn@0.05Si and Fe@Mn@0.05Si-c catalysts, we further explored the CO adsorption behavior on the two catalysts by in situ diffuse reflectance infrared Fourier transform spectroscopy (DRIFTS). Several bands at 2172, 2117, 1606, 1498, 1415, and 1364 cm^{-1} appeared on the Fe@Mn@0.05Si catalyst after CO adsorption (Fig. 5d). The doublet bands at 2172 and 2117 cm^{-1} was attributed to the vibrations of R-branch and P-branch of the gaseous CO on catalyst[36], which diminished fast upon sweeping in the Ar atmosphere (Fig. 5e). The bands located in the region of 1700 ~ 1200 cm^{-1} were assigned to carbonate species formed on the metal oxides[37–39]. The intensity of the bands at 1498 and 1364 cm^{-1} approached the maximum value within only 20 min after exposing to the CO atmosphere and then gradually decreased (Fig. 5f). Simultaneously, new bands at 1606 and 1415 cm^{-1} appeared and their intensity continuously increased, implying the formation of new sites for CO adsorption. This was attributed to that the adsorbed CO on catalyst surface had strong redox ability and led to the reduction of metal oxides, which was consistent with the results of in situ XRD. Besides, the intensity of these carbonate species still remained above 50% of its maximum value after sweeping in the Ar atmosphere for 120 min, suggesting that the adsorption ability of CO on the Fe@Mn@0.05Si catalyst was strong. In comparison, quite different CO adsorption behavior was observed on the Fe@Mn@0.05Si-c catalyst. Only gaseous CO and no carbonate species was detected (Fig. 5g–i), implying that CO could hardly adsorb on the catalyst containing chlorine.

Summarizing the information of in situ XRD and in situ DRIFTS characterizations, it could be deduced that chlorine could hinder the formation of Fe_xC active phase via inhibiting the adsorption of CO molecules. Moreover, chlorine also suppressed notably the reduction process of iron species by H_2 molecules (Supplementary Fig. 22). Thus, even exposing to the syngas atmosphere at reaction temperature, only Fe_3O_4 without Fe_xC existed in the catalyst containing chlorine, thereby leading to the deactivation of FTS catalyst. No chlorine element was detected on the Fe@Mn@0.2Si-c catalyst (Fig. 4f) and Fe_2O_3 converted

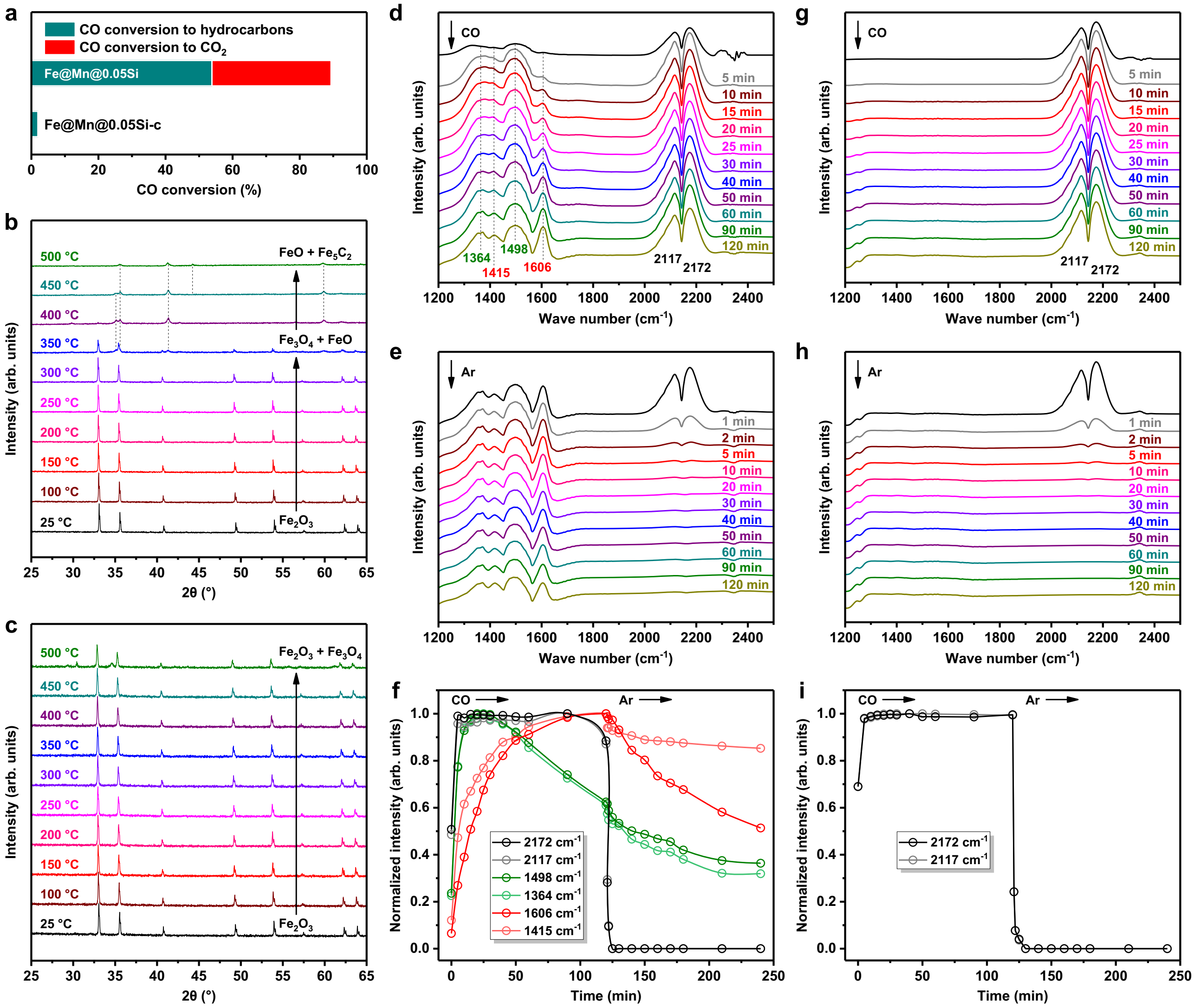

Fig. 5 | Effect of chlorine on the phase evolution and CO adsorption behavior. **a** CO conversion of catalysts. **b**, **c** In situ XRD patterns of the Fe@Mn@0.05Si (**b**) and Fe@Mn@0.05Si-c (**c**) catalysts in the 10%CO/90%N_2 atmosphere. **d**, **e**, **g**, **h** In situ DRIFTS spectra of CO adsorption on the Fe@Mn@0.05Si (**d**, **e**) and Fe@Mn@0.05Si-c (**g**, **h**) catalysts. The catalysts were exposed to the CO atmosphere at 320 °C for 120 min and then swept in the Ar atmosphere at 320 °C for another 120 min. **f**, **i** Normalized intensities of the surface species on the Fe@Mn@0.05Si (**f**) and Fe@Mn@0.05Si-c (**i**) catalysts as a function of time.

easily into iron carbide during reaction (Fig. 1), suggesting that appropriate thickness of SiO_2 shell could prevent the contact of hydrogen chloride with internal metal species during the hydrophobic modification procedure of catalyst synthesis and thus protect the catalyst from chlorine poisoning.

Discussion

In conclusion, we have investigated the effects of surface hydrophobization on the phase evolution behavior of iron-based FTS catalyst. The hydrophobic surface could reduce the water concentration in the core vicinity of catalyst during syngas conversion, thereby inhibiting the oxidation of iron species by water and stabilizing the Fe_xC active phase. As a result, the C − C coupling ability of catalyst was enhanced and more long-chain olefins were produced. The residual chlorine on catalyst during the hydrophobic modification procedure could poison the FTS catalyst by inhibiting the carbonization of iron species. The increase of SiO_2 shell thickness could protect catalyst from chlorine poisoning, while excessive SiO_2 inhibited the accessibility and carburization of internal iron species by CO molecules. Appropriate shell thickness was needed to stabilize the Fe_xC active phase without Fe_3O_4 formation and achieve good catalytic performance.

Methods

Catalyst preparation

The Fe_2O_3 was synthesized by a hydrothermal method. Typically, 7.5 g of iron trichloride hexahydrate ($FeCl_3·6H_2O$, AR) was dissolved in 110 mL of water. Then, 12.4 g of sodium acetate trihydrate ($CH_3COONa·3H_2O$, AR) and 3.8 g of hexadecyl trimethyl ammonium bromide ($C_{19}H_{42}BrN$, AR) were added. After stirring for 0.5 h, 26 mL of ethylenediamine ($C_2H_8N_2$, AR) was added. After stirring for 1 h, the solution was hydrothermally treated at 200 °C for 10 h. The product was washed with water and ethanol, dried at 100 °C for 12 h, and calcined at 500 °C for 5 h.

The Mn-promoted Fe_2O_3 was prepared by a deposition-precipitation method. Typically, 0.5 g of the prepared Fe_2O_3 was dispersed in 300 mL of ethanol (CH_3CH_2OH, AR) by ultrasonication. Then, 5 mL of aqueous solution containing 0.078 g of potassium permanganate ($KMnO_4$, AR) was added dropwise to the above suspension by a peristaltic pump. After stirring at 30 °C for 2 h, the product was collected by centrifugation, washed with water, and dried at 100 °C for 12 h. The obtained catalyst was named as Fe@Mn.

The hydrophilic SiO_2-coated catalysts were prepared by a modified Stöber method. Typically, 0.5 g of Fe@Mn was dispersed in 150 mL of ethanol by ultrasonication. Then, x mL ($x = 0.05, 0.2, 0.5, 1.0, 2.8$) of tetraethyl orthosilicate (TEOS, AR) was added. After stirring at 30 °C for 3 h, 2.5 mL of ammonia solution (25 ~ 28%, AR) and 10 mL of water were added. After stirring at 30 °C for 4 h, the product was collected by centrifugation, washed with ethanol, and dried at 100 °C for 12 h. The obtained hydrophilic catalysts were denoted as Fe@Mn@*x*Si.

The hydrophobic SiO_2-coated catalysts were prepared by further surface modification. Typically, 0.5 g of Fe@Mn@*x*Si was dried in a vacuum oven at 120 °C for 10 h. After cooling in the vacuum oven, 70 mL of *n*-hexane (C_6H_{14}, AR) was added. Subsequently, 0.5 mL of chlorotrimethylsilane (C_3H_9ClSi, ≥ 99.0%) was added. Then, the mixture was ultrasonic treated at room temperature for 1 h. The product was centrifuged, washed with *n*-hexane, and dried in a vacuum oven at 80 °C for 6 h. The obtained hydrophobic catalysts were denoted as Fe@Mn@*x*Si-c.

The Fe@Mn-c catalyst was prepared by similar procedures of Fe@Mn@*x*Si-c. Typically, 0.5 g of Fe@Mn was dried in a vacuum oven at 120 °C for 10 h. After cooling in the vacuum oven, 70 mL of *n*-hexane was added. Subsequently, 0.5 mL of chlorotrimethylsilane was added. Then, the mixture was ultrasonic treated at room temperature for 1 h. The product was centrifuged, washed with *n*-hexane, and dried in a vacuum oven at 80 °C for 6 h.

Catalyst characterization

The elemental composition of catalyst was determined by inductively coupled plasma (ICP) on an Agilent 5110 instrument. Transmission electron microscopy (TEM) and energy dispersive X-ray spectroscopy (EDS) elemental mapping images were obtained on a FEI Talos F200x instrument. Fourier transform infrared spectra (FTIR) was performed on a NICOLET 5700 FTIR Spectrometer. The powder sample was directly tested without pressing into a wafer with potassium bromide. Water-droplet contact angle tests were performed on a Kruss DSA100 contact angle goniometer.

X-ray photoelectron spectroscopy (XPS) of catalyst was recorded on a Thermo Scientific K-Alpha instrument and a Thermo Scientific ESCALAB Xi+ instrument. X-ray diffraction (XRD) pattern of catalyst was collected on an Ultima IV-185 diffractometer and a XPert Pro diffractometer with the 2θ range of 25° ~ 65°. The scanning step and rate were 0.02° and 10 °/min, respectively. The phases of catalyst were identified based on the JCPDS standard cards. Mössbauer spectrum of catalyst was obtained on wissel Mössbauer spectrometer.

Carbon monoxide temperature-programmed reduction (CO-TPR) experiments were performed on a DAS-7000 chemical adsorption instrument. Prior to each test, 50 mg of sample was packed into the quartz tube and pretreated with N_2 at 350 °C for 1 h. After cooling to 80 °C, $5\%CO/95\%N_2$ with a flow rate of 30 mL/min was switched into the quartz tube. Then, CO-TPR was conducted by ramping the temperature to 800 °C with a heating rate of 10 °C/min. The consumption of CO during the reduction process was detected by a thermal conductivity detector (TCD).

Hydrogen temperature-programmed reduction (H_2-TPR) experiments were performed on a DAS-7000 chemical adsorption instrument. Prior to each test, 50 mg of sample was packed into the quartz tube and pretreated with N_2 at 350 °C for 1 h. After cooling to 80 °C, 5% $H_2/95\%N_2$ with a flow rate of 30 mL/min was switched into the quartz tube. Then, H_2-TPR was conducted by ramping the temperature to 800 °C with a heating rate of 10 °C/min. The consumption of H_2 during the reduction process was detected by a TCD.

In situ XRD patterns of catalyst in the $CO + H_2O$ atmosphere were recorded on an Ultima IV-185 diffractometer equipped with a HT-XRD-900 reactor chamber (Beijing Scistar Technology Co., Ltd.). Before test, the iron species in catalyst were transformed into iron carbide by reduction in pure H_2 at 350 °C, 0.1 MPa for 20 h and carbonization in $31.6\%CO/68.4\%N_2$ at 320 °C, 2.0 MPa for 20 h. The powder sample without tabletting was packed into a ceramic sample stage in the reactor chamber. The $31.6\%CO/68.4\%N_2$ gas with a flow rate of 20 mL/min was switched into the reactor chamber, and H_2O was introduced in the reactor chamber by passing this gas through a glass wash bottle containing water at 40 °C. After exposing to the $CO + H_2O$ atmosphere at 320 °C, the XRD patterns of catalyst with the 2θ range of 29° ~ 79° were collected continuously, and the scanning step and rate were 0.02° and 5°/min, respectively.

In situ XRD patterns of catalyst in the $10\%CO/90\%N_2$ atmosphere were recorded on a Rigaku SmartLab diffractometer. About 100 mg of sample was loaded in a reaction chamber and then heated up from room temperature to 500 °C in $10\%CO/90\%N_2$ (20 mL/min). While the temperature was rising, the data were collected at 25 °C, 100 °C, 150 °C, 200 °C, 250 °C, 300 °C, 350 °C, 400 °C, 450 °C, 500 °C, respectively. The heating rate was 10 °C/min and the temperature was held for 10 min at each point before collecting data. The 2θ range and scanning rate were 25° ~ 65° and 10°/min, respectively.

In situ diffuse reflectance infrared Fourier transform spectroscopy (DRIFTS) was accomplished on a NICOLET iS50 FTIR Spectrometer. The powder sample was placed into an infrared cell and pretreated in the Ar atmosphere (30 mL/min) at 320 °C for 120 min with a heating rate of 5 °C/min. Then, the background spectrum was collected. Subsequently, the sample was exposed to the CO atmosphere (30 mL/min) at 320 °C for 120 min. Finally, the sample was swept in the Ar atmosphere (30 mL/min) at 320 °C for another 120 min.

Catalytic test

The syngas conversion reaction was performed in a stainless fixed-bed reactor (inner diameter = 10 mm, length = 40 cm). Typically, 0.5 g of catalyst diluted with 0.5 g of quartz sand was used. Prior to each reaction, the catalyst was reduced in pure H_2 at 350 °C and 0.1 MPa for 20 h and further activated with syngas at 320 °C and 0.1 MPa for 5 h. Then, the syngas conversion reaction was conducted at 320 °C, 2.0 MPa, 5000 $mL \cdot h^{-1} \cdot g^{-1}$ for 24 h, unless otherwise stated. The H_2/CO ratio in syngas was 2. The reaction products were detected by two gas chromatograph (FULI GC 97). One gas chromatograph was equipped with a TCD and a flame ionization detector (FID). Porapak Q and 5 A MolSieve packed column were connected to TCD, while RB-PLOT Al_2O_3 capillary column was connected to FID. The other gas chromatograph was equipped with a RB-5 capillary column and a FID. The carbon balance calculated was above 95%. The CO conversion and product selectivity were calculated on a carbon-atom basis. The catalytic data at the stable state after 12 h of reaction were collected and used for comparison.

The $CO + H_2O$ model experiment was performed in the same stainless fixed-bed reactor. Typically, 0.2 g of catalyst was packed into the reactor and firstly reduced in pure H_2 at 350 °C, 0.1 MPa for 20 h. Then, the catalyst was exposed to the CO or $CO + H_2O$ atmosphere at 320 °C, 2.0 MPa for 20 h. When co-feeding CO and H_2O in the reactor, liquid water with a flow rate of 0.002 mL/min was injected in the $31.6\%CO/68.4\%N_2$ gas (16.7 mL/min) via a high pressure constant current pump (eliteHPLC, EPP010S). The mixtures containing liquid water were vaporized in a gasifier at 300 °C before entering the reactor.

Data availability

The data that support the findings of this study are available within the paper and its Supplementary Information. The data generated in this study are provided in the Source Data file. Source data are provided with this paper.

References

1. Torres Galvis, H. M. et al. Supported iron nanoparticles as catalysts for sustainable production of lower olefins. *Science* **335**, 835–838 (2012).
2. Wang, C. et al. Fischer–Tropsch synthesis to olefins boosted by MFI zeolite nanosheets. *Nat. Nanotechnol.* **17**, 714–720 (2022).
3. Zhong, L. et al. Cobalt carbide nanoprisms for direct production of lower olefins from syngas. *Nature* **538**, 84–87 (2016).
4. Fang, W. et al. Physical mixing of a catalyst and a hydrophobic polymer promotes CO hydrogenation through dehydration. *Science* **377**, 406–410 (2022).
5. Yu, H. et al. Direct production of olefins from syngas with ultrahigh carbon efficiency. *Nat. Commun.* **13**, 5987 (2022).
6. Li, J. et al. Integrated tuneable synthesis of liquid fuels via Fischer–Tropsch technology. *Nat. Catal.* **1**, 787–793 (2018).
7. Xiao, J. et al. Tandem catalysis with double-shelled hollow spheres. *Nat. Mater.* **21**, 572–579 (2022).
8. Zhou, W. et al. New horizon in C1 chemistry: breaking the selectivity limitation in transformation of syngas and hydrogenation of CO_2 into hydrocarbon chemicals and fuels. *Chem. Soc. Rev.* **48**, 3193–3228 (2019).
9. Zhai, P. et al. Development of direct conversion of syngas to unsaturated hydrocarbons based on Fischer-Tropsch route. *Chem* **7**, 3027–3051 (2021).
10. Chang, Q. et al. Relationship between iron carbide phases (ε-Fe_2C, Fe_7C_3, and χ-Fe_5C_2) and catalytic performances of Fe/SiO_2 Fischer–Tropsch catalysts. *ACS Catal.* **8**, 3304–3316 (2018).
11. Lyu, S. et al. Stabilization of ε-iron carbide as high-temperature catalyst under realistic Fischer–Tropsch synthesis conditions. *Nat. Commun.* **11**, 6219 (2020).
12. Zhu, J. et al. Dynamic structural evolution of iron catalysts involving competitive oxidation and carburization during CO_2 hydrogenation. *Sci. Adv.* **8**, eabm3629 (2022).
13. Pirola, C., Bianchi, C. L., Di Michele, A., Vitali, S. & Ragaini, V. Fischer Tropsch and Water Gas Shift chemical regimes on supported iron-based catalysts at high metal loading. *Catal. Commun.* **10**, 823–827 (2009).
14. van der Laan, G. P. & Beenackers, A. Intrinsic kinetics of the gas-solid Fischer-Tropsch and water gas shift reactions over a precipitated iron catalyst. *Appl. Catal. A-Gen.* **193**, 39–53 (2000).
15. Zhao, H. et al. Synthesis of iron-carbide nanoparticles: Identification of the active phase and mechanism of Fe-based Fischer-Tropsch synthesis. *CCS. Chemistry* **3**, 2712–2724 (2021).
16. Cheng, Y. et al. Mg and K dual-decorated Fe-on-reduced graphene oxide for selective catalyzing CO hydrogenation to light olefins with mitigated CO_2 emission and enhanced activity. *Appl. Catal. B-Environ.* **204**, 475–485 (2017).
17. Gong, H. et al. Fe-Sn bimetallic catalysts for an enhanced Fischer-Tropsch synthesis stability via oxygen removal and coking resistance. *Fuel* **311**, 122115 (2022).
18. Wang, P. et al. Synthesis of stable and low-CO_2 selective ε-iron carbide Fischer-Tropsch catalysts. *Sci. Adv.* **4**, eaau2947 (2018).
19. Xu, Y. et al. A hydrophobic FeMn@Si catalyst increases olefins from syngas by suppressing C1 by-products. *Science* **371**, 610–613 (2021).
20. Shi, Y. et al. Hydrophobic Fe-based catalyst derived from prussian blue for enhanced photothermal conversion of syngas to light olefins. *Adv. Funct. Mater.* **34**, 2308670 (2024).
21. Li, S. et al. Fischer-Trospch to olefins over hydrophobic $FeMnO_x$@SiO_2 catalysts: the effect of SiO_2 shell content. *Appl. Catal. A-Gen.* **635**, 118552 (2022).
22. Tan, M. et al. Probing hydrophobization of a Cu/ZnO catalyst for suppression of water–gas shift reaction in syngas conversion. *ACS Catal.* **11**, 4633–4643 (2021).
23. Chen, G. et al. Hydrophobic dual metal silicate nanotubes for higher alcohol synthesis. *Appl. Catal. B-Environ.* **334**, 122840 (2023).
24. Xu, Y. et al. Insights into the diffusion behaviors of water over hydrophilic/hydrophobic catalysts during the conversion of syngas to high-quality gasoline. *Angew. Chem. Int. Ed.* **62**, e202306786 (2023).
25. Zhang, Z. et al. Unraveling the role of Fe_5C_2 in CH_4 formation during CO_2 hydrogenation over hydrophobic iron catalysts. *Appl. Catal. B-Environ.* **327**, 122449 (2023).
26. Liu, X., Lin, T., Liu, P. & Zhong, L. Hydrophobic interfaces regulate iron carbide phases and catalytic performance of $FeZnO_x$ nanoparticles for Fischer-Tropsch to olefins. *Appl. Catal. B-Environ.* **331**, 122697 (2023).
27. Yu, X. et al. Fischer-Tropsch synthesis over methyl modified Fe_2O_3@SiO_2 catalysts with low CO_2 selectivity. *Appl. Catal. B-Environ.* **232**, 420–428 (2018).
28. Zhang, J. et al. Switching of CO_2 hydrogenation selectivity via chlorine poisoning over Ru/TiO_2 catalyst. *Nano Res* **16**, 4786–4792 (2023).
29. Paredes-Nunez, A., Lorito, D., Schuurman, Y., Guilhaume, N. & Meunier, F. C. Origins of the poisoning effect of chlorine on the CO hydrogenation activity of alumina-supported cobalt monitored by operando FT-IR spectroscopy. *J. Catal.* **329**, 229–236 (2015).
30. Li, W. et al. The effect of chlorine modification of precipitated iron catalysts on their Fischer–Tropsch synthesis properties. *Catalysts* **12**, 812 (2022).
31. Bambal, A. S., Guggilla, V. S., Kugler, E. L., Gardner, T. H. & Dadyburjor, D. B. Poisoning of a silica-supported cobalt catalyst due to presence of sulfur impurities in syngas during Fischer-Tropsch synthesis: effects of chelating agent. *Ind. Eng. Chem. Res.* **53**, 5846–5857 (2014).
32. Ma, W. et al. Fischer-Tropsch synthesis: effect of ammonia in syngas on the Fischer-Tropsch synthesis performance of a precipitated iron catalyst. *J. Catal.* **326**, 149–160 (2015).
33. Ma, W. et al. Fischer–Tropsch synthesis: effects of hydrohalic acids in syngas on a precipitated iron catalyst. *ACS Catal.* **5**, 3124–3136 (2015).
34. van Steen, E. & Claeys, M. Fischer-Tropsch catalysts for the Biomass-to-Liquid process. *Chem. Eng. Technol.* **31**, 655–666 (2008).
35. Leibold, H., Hornung, A. & Seifert, H. HTHP syngas cleaning concept of two stage biomass gasification for FT synthesis. *Powder Technol.* **180**, 265–270 (2008).
36. Sarkodie, B. et al. Boosting the efficiency of low-loaded Au on spongy Fe_2O_3 via interfacial ferric hydroxide for low-temperature CO oxidation. *Mater. Chem. Phys.* **288**, 126407 (2022).
37. Ding, M. et al. Study on reduction and carburization behaviors of iron phases for iron-based Fischer-Tropsch synthesis catalyst. *Appl. Energy* **160**, 982–989 (2015).
38. Jiang, M., Koizumi, N. & Yamada, M. Adsorption properties of iron and iron–manganese catalysts investigated by in-situ diffuse reflectance FTIR. *Spectrosc. J. Phys. Chem. B.* **104**, 7636–7643 (2000).
39. Zhu, Y. et al. Role of manganese oxide in syngas conversion to light olefins. *ACS Catal.* **7**, 2800–2804 (2017).

Acknowledgements

This work was supported by the National Key R&D Program of China (2022YFB4101201 received by Y.X.), National Natural Science Foundation of China (22302149 and 52376206 received by Y.X.), Natural Science Foundation of Jiangsu Province (BK20230267 received by Y.X.), Innovative Groups in Hubei Province (2022CFA017 received by M.D.), Natural Science Foundation of Hubei Province (2023AFB051 received by Y.X.), Knowledge Innovation Project of Wuhan (2023020201020251 received by Y.X.), Fundamental Research Funds for the Central Universities (2042023kf0106 received by Y.X.), Foundation of State Key Laboratory of Coal Conversion (J23-24-610 received by Y.X.), China National Postdoctoral Program for Innovative Talents (BX20220242 received by Y.X.), China Postdoctoral Science Foundation (2023M732693 received by Y.X.), and the Xiaomi Foundation/Xiaomi Young Talents Program received by Y.X.

Author contributions

Y.X. and M.D. conceived and supervised the project, designed the study. Y.X. performed most of the experiments. Z.Z., K.W., R.S., and L.L. conducted some catalytic evaluation experiments. J.W. and B.H. provided some idea and experimental guidance. Y.X. and M.D. wrote the manuscript with input from all the authors.

Competing interests

The authors declare no competing interests.

Additional information

Supplementary information The online version contains supplementary material available at https://doi.org/10.1038/s41467-024-51472-w.

Correspondence and requests for materials should be addressed to Yanfei Xu or Mingyue Ding.

Peer review information *Nature Communications* thanks the anonymous reviewer(s) for their contribution to the peer review of this work. A peer review file is available.

Reprints and permissions information is available at http://www.nature.com/reprints

Publisher's note Springer Nature remains neutral with regard to jurisdictional claims in published maps and institutional affiliations.

Open Access This article is licensed under a Creative Commons Attribution-NonCommercial-NoDerivatives 4.0 International License, which permits any non-commercial use, sharing, distribution and reproduction in any medium or format, as long as you give appropriate credit to the original author(s) and the source, provide a link to the Creative Commons licence, and indicate if you modified the licensed material. You do not have permission under this licence to share adapted material derived from this article or parts of it. The images or other third party material in this article are included in the article's Creative Commons licence, unless indicated otherwise in a credit line to the material. If material is not included in the article's Creative Commons licence and your intended use is not permitted by statutory regulation or exceeds the permitted use, you will need to obtain permission directly from the copyright holder. To view a copy of this licence, visit http://creativecommons.org/licenses/by-nc-nd/4.0/.

© The Author(s) 2024